ACS OMEGA

Open Access

http://pubs.acs.org/journal/acsodf

Article

Direct or Indirect Sonication in Ecofriendly MoS_2 Dispersion for NO_2 and NH_3 Gas-Sensing Applications

Dalal Fadil,* Jyayasi Sharma, Mubdiul Islam Rizu, and Eduard Llobet

Cite This: *ACS Omega* 2024, 9, 25297−25308

Read Online

ACCESS | Metrics & More | Article Recommendations | Supporting Information

ABSTRACT: Unlike the most used, this study explores the effects of direct and indirect sonication methods on the dispersion and gas sensing performance of MoS_2 nanoflakes. The obtained dispersions are characterized using various techniques, such as field emission scanning electron microscopy, high resolution transmission electron microscopy, atomic force microscopy, dynamic light scattering, and Raman and X-ray diffraction, to evaluate their morphological and structural properties. Gas sensing measurements are conducted using exfoliated MoS_2 on interdigitated electrode structures, and the response to multiple gases is recorded. The sensitivity and selectivity of the sensors are analyzed and compared between the direct and indirect sonication methods. The results demonstrate that both direct and indirect methods lead to the formation of well-dispersed MoS_2 multilayer nanosheets, whereas the indirect approach exhibits a uniform and bigger flake size. Gas sensing experiments reveal that the MoS_2 nanoflakes prepared via indirect sonication have enhanced sensitivity by 17 and 46% toward NO_2 and NH_3 gases, respectively, compared to the ones achieved by the direct sonication method. Both methods demonstrated its selectivity for NO_2 and NH_3 and the preferential temperature to detect NO_2 and NH_3 gas are 50 and 100 °C, respectively. This research contributes to the development of eco-friendly MoS_2-based gas sensors by providing insights into the influence of direct (probe) and indirect (bath) sonication methods on dispersion quality and gas sensing performance. The findings highlight the potential of indirect sonication as a reliable technique for fabricating high-performance MoS_2 gas sensors, opening venues for the design and optimization of eco-friendly sensing platforms for environmental monitoring and industrial applications.

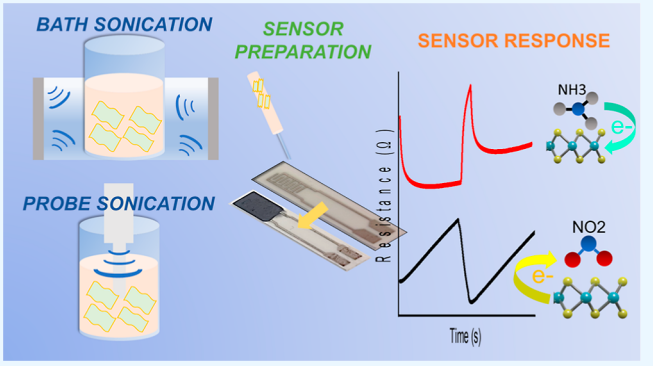

1. INTRODUCTION

Gas sensors have a wide range of applications in industries such as healthcare, food processing, transport, and public safety (homes, schools, offices, etc.).[1,2] In fact, the use of sensors to detect explosive or toxic gases is inevitable in the chemical or petrochemical industries. Even in hospitals, it is necessary to use gas sensors for the breath monitoring system, lung function diagnosis, and monitoring CO_2 levels.[3] Sensors are used for controlling the amount of oxygen in the air and maintaining the conditions of food storage.[4] They are needed in automotive exhaust systems to limit NOx emissions and control the antipollution system.[5] For public safety, it is necessary to check air quality, prevent against fire and toxic gases, and to detect pollutants (NO_2, NO, CO, CO_2, and NH_3) in the atmosphere. The World Health Organization reported in 2021 that 7 million deaths every year were directly related to exposure to ambient air pollution. In particular, NO_2 and NH_3 are two species that need to be monitored in our environment. NO_2 is an indirect greenhouse gas that causes asthma, eutrophication, and even cardiovascular mortality. The maximum permitted exposure limit is 1 ppm during 15 min and 0.5 ppm (500 ppb) during 8 h, which require highly sensitive gas sensors with low detection limits. NH_3 is a toxic gas; its maximum permissible exposure limit is 50 ppm during 15 min and 20 ppm during 8 h.[6,7]

There are different types of gas sensors employing different transduction schemes.[8,9] One of the most successful transducing approaches is chemoresistive. It is simple and easy to fabricate. It consists of measuring the resistance variation of a gas-sensitive film/coating as a function of gas concentrations. The most employed materials used for detecting gas are metal oxides (ZnO, SnO_2, WO_3, and TiO_2, only to cite a few) because of their good sensitivity and low cost.[1] However, the need for low-power gas sensors that can operate at temperatures close to room temperature maintaining keeping good sensitivity, selectivity, and stability has promoted new investigations on two-dimensional (2D) materials, including transition metal dichalcogenide materials.[8,10] Molybdenum

Received: April 2, 2024
Revised: May 14, 2024
Accepted: May 22, 2024
Published: June 3, 2024

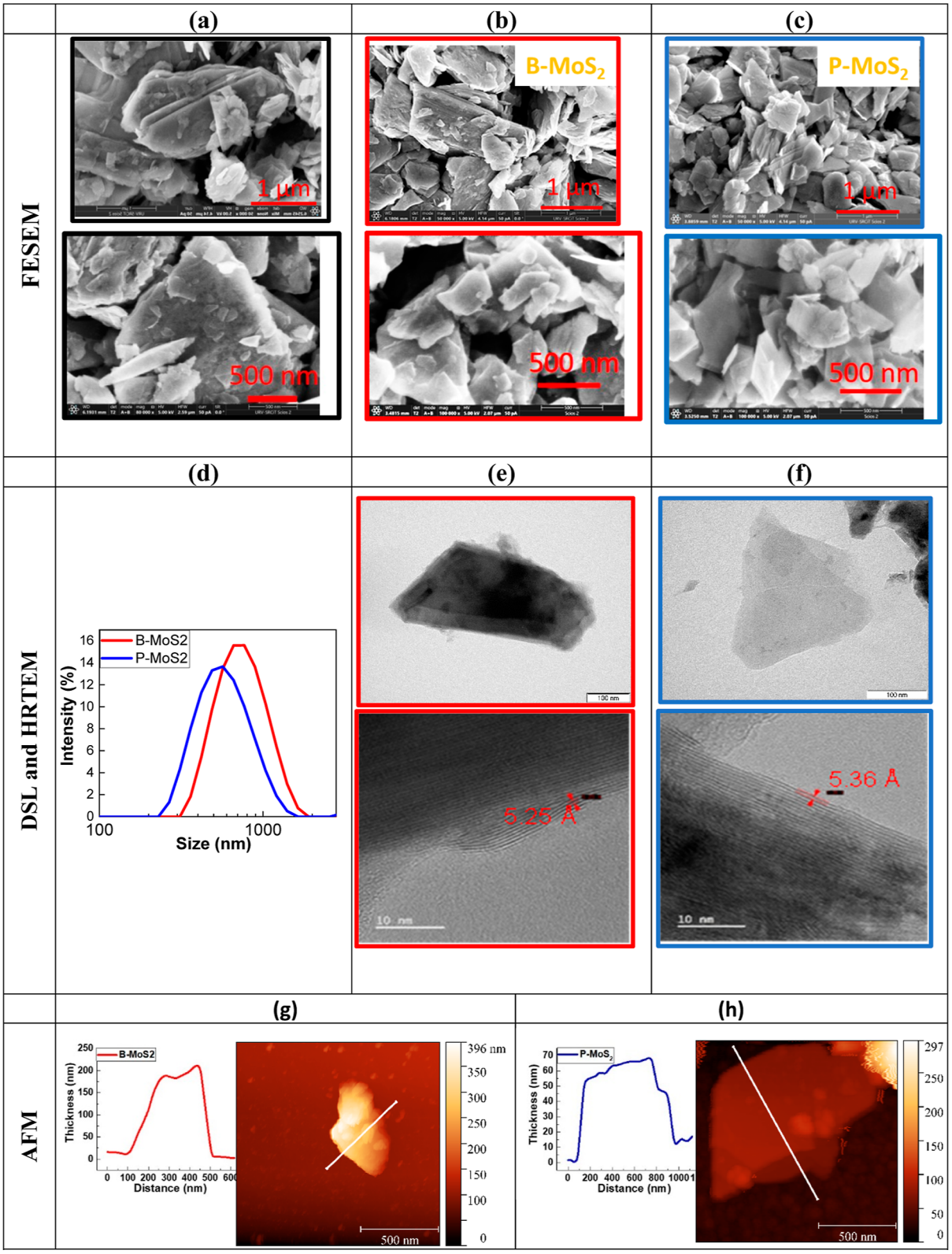

Figure 1. FESEM images illustrating: (a) MoS_2 initial powder, (b) nanosheets obtained via bath sonication B-MoS_2, and (c) nanosheets produced by probe sonication P-MoS_2 in the lower part of the dispersion. Scale bars represent length of 1 μm (top) and 500 nm (bottom). (d) DLS for size analysis comparing B-MoS_2 and P-MoS_2 nanosheets. (e,f) High-resolution TEM images of exfoliated MoS_2 featuring 100 nm scale bares for both multilayered B-MoS_2 and P-MoS_2 nanosheets, along with the corresponding interlayer spacing in the edges of the crystallites. AFM image of B-MoS_2 and P-MoS_2 nanosheets, including 500 nm scale bares with associated height profiles along the white line in (g,h), respectively.

disulfide MoS_2 is one of the TMDs that deserves to be well studied. It has a tunable band gap, a large surface-to-volume ratio, and good selectivity, and it shows potential for being operated at low temperatures, which is promising for

https://doi.org/10.1021/acsomega.4c03166
ACS Omega 2024, 9, 25297−25308

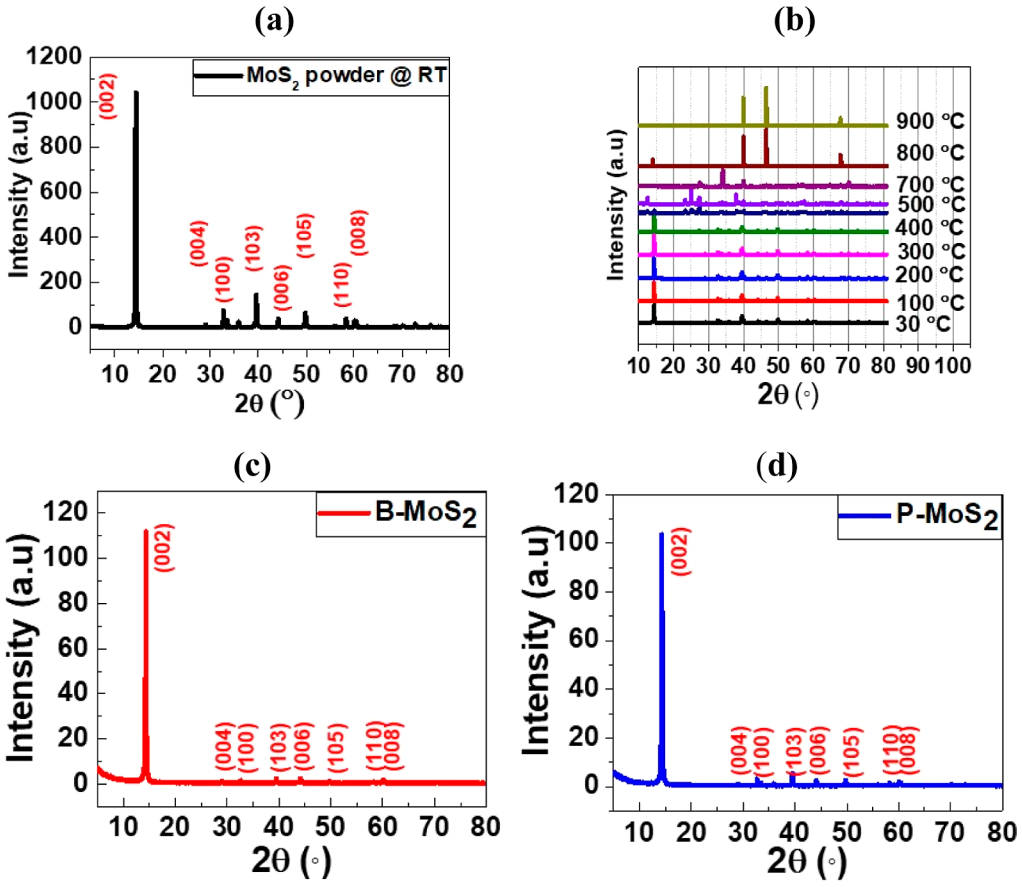

Figure 2. (a,b) XRD spectra of MoS_2 powder captured at room temperature and at various temperature intervals ranging from 30 to 900 °C, in an increment of 100 °C under ambient atmospheric conditions. (c,d) XRD analysis of the lower part of the dispersion after exfoliation of MoS_2 using bath sonication (B-MoS_2) and probe sonication (P-MoS_2) deposited by drop casting on a silicon substrate.

developing new gas sensing applications. The weak van der Waals interaction between layers in MoS_2 materials allows them to be chemically exfoliated from bulk crystals, shearing the layers to yield nanosheets and even monolayers in solution.[11−14] This approach is low-cost and efficient for achieving large-scale production of 2D materials in solution and can provide a sustainable route to the production of 2D nanosheets for device production and commercialization. To disperse MoS_2 in solution, two approaches to ultrasonication are commonly used to separate the bulk crystal into 2D nanosheets through high-energy jets that provide mechanical agitation concurrent with the chemical action engendered by the dispersion solvent. Probe sonication uses an ultrasound probe to transmit the high-frequency vibrations generated directly from the sample. This method is relatively straightforward and is commonly used for dispersion. Bath sonication is an indirect sonication method in which the ultrasonication energy travels from the horn through the water bath and to the sample that is held in a vial. The high-intensity ultrasound energy promotes the exfoliation of 2D materials. It was reported on graphene oxide that probe sonication induces deformation between layers and causes more rugosities and degradation of the morphology of the material. However, bath sonication is less invasive, enables easy control of the sample temperature, and causes fewer wrinkles and less damage to the sheet structure and morphology of the 2D material in comparison to probe sonication.[15]

Besides sonication, the choice of solvent is also an important factor in determining the effectiveness of the dispersion. As demonstrated by Coleman et al.,[12] solvents like *N*-methyl 2-pyrrolidone (NMP) are suitable for MoS_2 dispersion because their surface tension is close to that of MoS_2 surface tension; however, they are toxic and difficult to remove. On the other hand, solvents like IPA, acetone, and ethanol are low-cost and environmentally friendly alternatives with low surface tension. Their association with water promotes MoS_2 dispersion.[16−19] In the literature, few studies have been conducted on MoS_2 dispersion for gas sensing. Most of the reported MoS_2 gas sensors are made of exfoliated nanosheets collected from the supernatant of dispersion and prepared by probe sonication, either at low-time sonication (1 or 2 h) by using a toxic solvent like NMP or at long-time sonication (8 or 24 h) by using a solvent.

The development of ecofriendly materials for gas sensors has gained significant attention due to their potential impact on environmental sustainability and human health. Sonication has emerged as a promising technique to disperse MoS_2 or any two-dimensional materials in liquid preparation involving the separation from bulk to nanosheets, which induces a large surface-to-volume ratio and strong surface activities affecting the performance of gas sensors. Both direct (probe) and indirect (bath) sonication methods are employed. Is there any one preferable for sensing gas? In this work, we provided gas sensor results of multilayer 2D MoS_2 collected from the sediment of the dispersion prepared on the one side by probe

https://doi.org/10.1021/acsomega.4c03166
ACS Omega 2024, 9, 25297−25308

sonication (P-MoS_2) and on the other side by bath sonication (B-MoS_2) employing reasonable sonication time and dispersed in eco-friendly solvents.

2. RESULTS AND DISCUSSION

The sensing behavior of MoS_2 nanosheets is significantly influenced by the morphology, the number of active sites, and defects in the form of vacancies. To analyze the surface morphology and the structure of the MoS_2 after sonication, field emission scanning electron microscopy (FE-SEM) (FEI company), high resolution transmission electron microscopy (HR-TEM), dynamic light scattering (DLS), atomic force microscopy (AFM), X-ray diffraction analysis XRD (Bruker D8), and Raman spectroscopy (Renishaw inVia) were used.

2.1. FESEM, HR-TEM, DSL, and AFM. Field emission scanning electron microscopy (FESEM) images of the MoS_2 powder before and after sonication are presented in Figure 1. The initial powder was mixed with distilled water and deposited on a silicon substrate. It shows thick stacked flakes with different sizes, thicknesses, and nonuniform triangle or rectangle shapes of bulk material (Figure 1a). After sonication and centrifugation, as described above, the bottom part of the dispersion was deposited on interdigitated alumina substrates for gas sensing measurements. Multilayer flakes can be observed. Comparing to the initial bulk powder, exfoliated MoS_2 by bath sonication B-MoS_2 (Figure 1b) shows less damage to the flakes and preserves the later size estimated in average to some micrometers. In contrast, probe-sonicated P-MoS_2 flakes (Figure 1c) show a reduction in the later size estimated to be on average about 500 nm. To explore the lateral size of the prepared dispersion, dynamic light scattering (DSL) was performed with Zetasizer-Ultra Malvern Instruments. DLS works by illuminating particles with a laser and analyzing the intensity fluctuations in the scattering light. The solution was placed in a standard glass cuvette, and the size measurement was acquired by ZS XPLORER software. Figure 1d presents the particle size distribution for B-MoS_2 and P-MoS_2 dispersions samples. The lateral size of B-MoS_2 ranges from 300 to 2000 nm, and that of P-MoS_2 is about 230 to 1400 nm, confirming the FESEM observations. High-resolution-TEM imaging was conducted by a JEOL F200 instrument. Extracted nanosheets of B-MoS_2 and P-MoS_2 are illustrated in Figure 1e,f, respectively. It clearly shows that for B-MoS_2 (Figure 1e), large rectangular nanoplatelets above 400 nm in lateral dimensions are present, while the P-MoS_2 sample (Figure 1f) shows triangular nanosheets to be much smaller on average. The morphology reveals large platelets in B-MoS_2, as confirmed by FESEM and DSL analysis. The interplanar spacing indicates the distance between two adjacent sulfur layers in the same single layer of MoS_2. The extracted values are 5.25 Å for B-MoS_2 and 5.36 Å for P-MoS_2, corresponding to the (002) plane in MoS_2, which is close to the interplanar spacing of monolayer MoS_2 (approximatively 6.15 Å).[20,21] The presence of multiple lines at the edge reveals that both methods result in multilayer MoS_2 nanosheets. To evaluate the thickness of the nanosheets, we used the AFM technique. The height profile of an individual B-MoS_2 nanosheet is found to be 200 nm in Figure 1g. This value is higher than the one expected by the XRD technique, indicating the existence of nonexfoliated material or the occurrence of agglomeration at the bottom of the dispersion; in contrast, the value for P-MoS_2 (70 nm) in Figure 1h is close to the value calculated with the XRD technique. To sum up, thick nanosheets are observed in both types of samples; however, wider nanosheets are obtained in B-MoS_2 compared to P-MoS_2.

2.2. X-ray Diffraction. X-ray diffraction studies of the MoS_2 powders were carried out at room temperature, and the results are presented in Figure 2a. The XRD peaks appeared at the expected 2θ angles of 14.39, 29.02, 32.69, 39.56, 44.16, 56.02, 58.35, and 60.16°, which correspond respectively to (002), (004), (100), (103), (006), (106), (110), and (008) crystallographic planes with MoS_2, the most prominent peak resulting from the (002) plane. MoS_2 has a hexagonal structure and belongs to the $P6_3/mmc$ (194) space group. The lattice parameters of MoS_2 are $a = b = 3.16020$ Å and $c = 12.29400$ Å, according to PDF card number 65-1951.

To study the stability of the MoS_2 powder regarding temperature variation, the XRD of the MoS_2 initial powder was measured after heating from 30 to 900 °C in atmospheric air. Figure 2b indicates that MoS_2 is stable up to 400 °C. From 500 °C, the peak (002) decreases and disappears at 600 °C. Other new peaks appeared at $2\theta \sim$ 12.49, 23.25, 25.16, 27.14, 33.77, 38.07, 40.05, 45.62, 46.56, 49.44, 57.63, and 67.90°. At 900 °C, only three principal peaks remain at 39.95, 49.44, and 67.9°. It was reported that peaks at 23.25, 49.44, and 57.63° could be related to the (110), (200), and (112) planes of MoO_3 orthorhombic crystal structure, respectively. Some other peaks could be attributed to hexagonal molybdenum trioxide MoO_3.[22,23] Also, some peaks can be shifted due to the strain and size effects or decomposition of MoS_2 at high temperatures.[24]

From Figure 2c,d, exfoliated MoS_2 was deposited onto a silicon wafer by using drop casting and subsequently dried. X-ray Diffraction of MoS_2 powder crystal and exfoliated MoS_2 through bath and probe sonication was performed at room temperature in the 2θ range between 5 and 80°. As reported previously in ref 25, the intensity of the (002) peak after exfoliation is lower than in the bulk material due to the exfoliation process. From Figure 2, and after compensating for the instrument effect, we extracted the interplanar distance "d" of the (002) plane using the PDF card number 00-037-1492 and the Bragg equation $d = n\lambda/2 \sin\theta$, where "$d$" represents the atomic plane spacing, "n" stands for the diffraction order, "λ" denotes the incident radiation wavelength, and "θ" signifies the diffraction angle. The determined interplanar spacing values are as follows: d(Bulk) = 6.14544 ± 0.00019 Å, which is marginally smaller than the interplanar spacing of exfoliated MoS_2 obtained through bath sonication (d(B-MoS_2) = 6.1767 ± 0.0003 Å) and probe sonication (d(P-MoS_2) = 6.1755 ± 0.0003 Å). This slight increase in interplanar spacing is potentially due to the presence of water between MoS_2 layers or the restacking of MoS_2 layers that occurred during XRD sample preparation.[26]

Additionally, according to the PDF 00-037-1492, we calculated the average crystallite sizes "D" based on the Debye−Scherrer equation: $D = k\lambda/(\beta \cos\theta)$. Here, "$\lambda$" corresponds to the X-ray wavelength (0.154 nm), "k" is a constant (equal to 1), "β" represents the integral breadth at (002) peak, and "θ" is the diffraction angle. Consequently, we determined the average crystallite size of the bulk powder to be D(MoS_2) = 60.7 ± 7 nm. Postexfoliation, the (002) peak displayed greater broader (β was higher), leading to a crystallite size of 47.7 ± 6 nm for B-MoS_2 and 47.0 ± 7 nm for P-MoS_2. These reduced sizes in the B-MoS_2 and P-MoS_2 samples confirmed the successful exfoliation of the material. Similar to the methodology employed in ref 26, we calculated

https://doi.org/10.1021/acsomega.4c03166
ACS Omega 2024, 9, 25297−25308

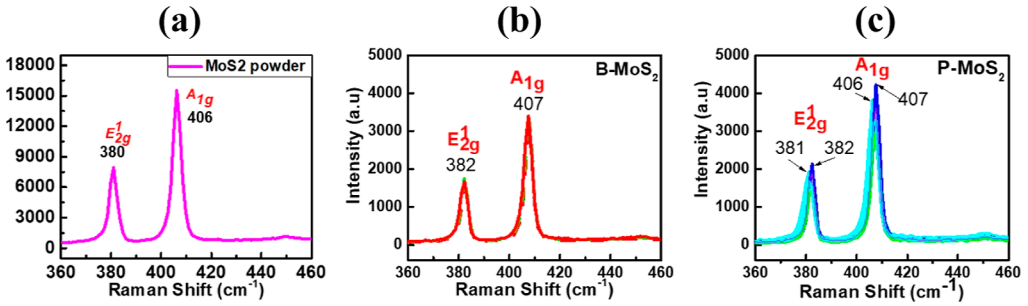

Figure 3. (a) Raman spectrum illustrating the characteristics of MoS_2 powder. Comparative Raman spectra from distinct sensor regions are overlaid for (b) bath sonication (depicted in black and red) and (c) probe sonication (shown in blue and cyan). The values corresponding to the in-plane $^1E_{2g}$ and out-of-plane A_{1g} modes are highlighted within each spectrum.

the number of layers per particle by dividing the crystallite size by the interplanar distance of (002) value. Consequently, the number of MoS_2 layers decreased from 98 layers for bulk material to 77 layers for B-MoS_2 and 76 layers per particle for P-MoS_2.

2.3. Raman Spectroscopy. Structural information was obtained by Raman spectroscopy (Renishaw inVia

instrument) using a 514 nm laser wavelength in air under ambient conditions. Before measuring, the spectrometer was first calibrated to a silicon reference sample to correct the instrument response, and then our samples were introduced. The Raman emission was collected by a 50× long working distance objective lens at magnification in the streamline mode and dispersed by a 2400 line/mm grating. Laser power was selected in such a way to avoid any overheating and damage to the surface with 0.5% of the laser power in the wavenumber region 360−460 cm^{-1}. MoS_2 coatings already deposited on the alumina transducing substrates were employed for Raman and sensor characterizations. The $^1E_{2g}$ Raman peak position and the distance between peaks indicate the layer number.[27−29] The distance between the peaks is 26 cm^{-1} for bulk material (Figure 3a), while it is equal to 25 cm^{-1} after sonication for B-MoS_2 (Figure 3b) and P-MoS_2 (Figure 3c), indicating the presence of thick nanosheets and the lowering in the thickness of MoS_2 nanosheets for sonicated materials, which is in agreement with the AFM and XRD analysis results discussed above. The blue shift of the $^1E_{2g}$ peak from 380 to 382 cm^{-1} confirms the exfoliation and the lowering in the number of layers. On the other hand, the shift of the $^1E_{2g}$ mode can be attributed to Coulomb interactions from the coupled dipoles induced by Mo−S bonds, as reported by Yang et al.[20] The Coulomb interactions tend to decrease the frequency of $^1E_{2g}$. An increase in the number of layers leads to stronger Coulomb forces and stronger interlayer interactions. In the B-MoS_2 and P-MoS_2 samples, the Coulomb interaction is probably smaller than the interlayer interactions. Sonication may induce a small residual strain in the discontinuous nanosheets, which induces a blue shift in $^1E_{2g}$ and A_{1g}. The blue shift of the A_{1g} peak after sonication can be attributed to the tensile strain or the p-type nature of MoS_2.[20,30]

2.4. UV−Visible. It is well known that MoS_2 bulk material has an indirect bandgap of 1.2 eV, whereas MoS_2 monolayer is a direct bandgap semiconductor with an increased bandgap value of 1.8 to 1.9 eV.[31] Here, absorption measurements were recorded on a SECOMAM UViline9600 spectrophotometer in the range of 250 to 1100 nm. The signal is noisy because the very concentrated sample from the bottom of the dispersion induces a lot of absorbance noise. We observed in Figure 4a

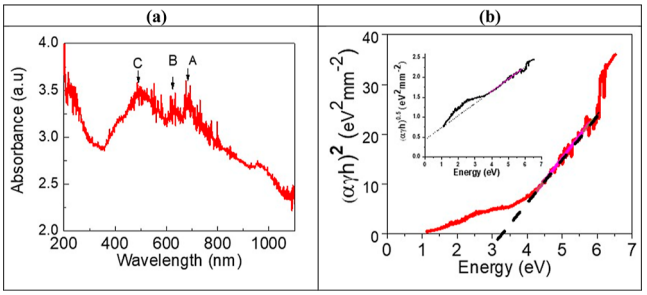

Figure 4. (a) Absorbance as a function of the wavelength of B-MoS_2. (b) Tauc's plot for B-MoS_2 and the intercept of the linear fit (dot line) with the horizontal axis defines the value of the band gap. In the inset is the indirect band gap.

three excitonic peaks at 681 nm (1.82 eV), 632 nm (1.96 eV), and 503 nm (2.46 eV) corresponding to A, B, and C excitons. The A and B peaks arise from direct exitonic transitions at the *K* point of the Brillouin zone. The C peak can be assigned to the direct excitonic transition of the M point. The absorbance peaks are consistent with previous results by Fadil et al.[19] The band gap BG was extracted by using Tauc plot, as specified in ref 19. The indirect band gap formula $(\alpha\ h\ \gamma)^n$ with the exponent equal to 1/2 was verified and presented in the inset of Figure 4b. The linear extrapolation did not intersect with the energy axis. Thus, we plot the direct band function $(\alpha\ h\ \gamma)^2$ as a function of the energy. Where α = 2.303 A/d from the Lambert−Beer−Lambert law. Here, d = 10 mm is the path length of the cuvette, A represents the absorbance value, h is Planck's constant, and γ is the incoming photon frequency in the spectrophotometer. The extracted band gap of the B-MoS_2 nanosheets is 3.3 eV, close to the predicted BG value of 2.8 eV for monolayer MoS_2, within the GW band gap approximation.[32] The particle size can be estimated from the Figure 4a spectrum using the formula in ref 33. Here, the absorbance at the B peak is equal to 3.38, and the absorbance at 352 nm is 2.87. The calculated particle size was 286 nm, and the number of layers was estimated at 22.8, confirming the exfoliation. These values are in the same order of magnitude as those obtained via the DLS, AFM, and XRD studies reported above.

2.5. Sensor Response. Figure 5a,b shows the variation of the resistance at 50 °C resulting from exposure of the sensors to NO_2 gas concentrations ranging from 40 to 800 ppb and NH_3 gas concentrations from 3 to 10 ppm for both B-MoS_2 and P-MoS_2 sensors. These figures illustrate the final cycle of reproducibility, as shown in Figure S1. Sensor resistance shows a p-type semiconducting behavior, with the majority of charge carriers being holes for both types of devices. The resistance

https://doi.org/10.1021/acsomega.4c03166
ACS Omega 2024, 9, 25297−25308

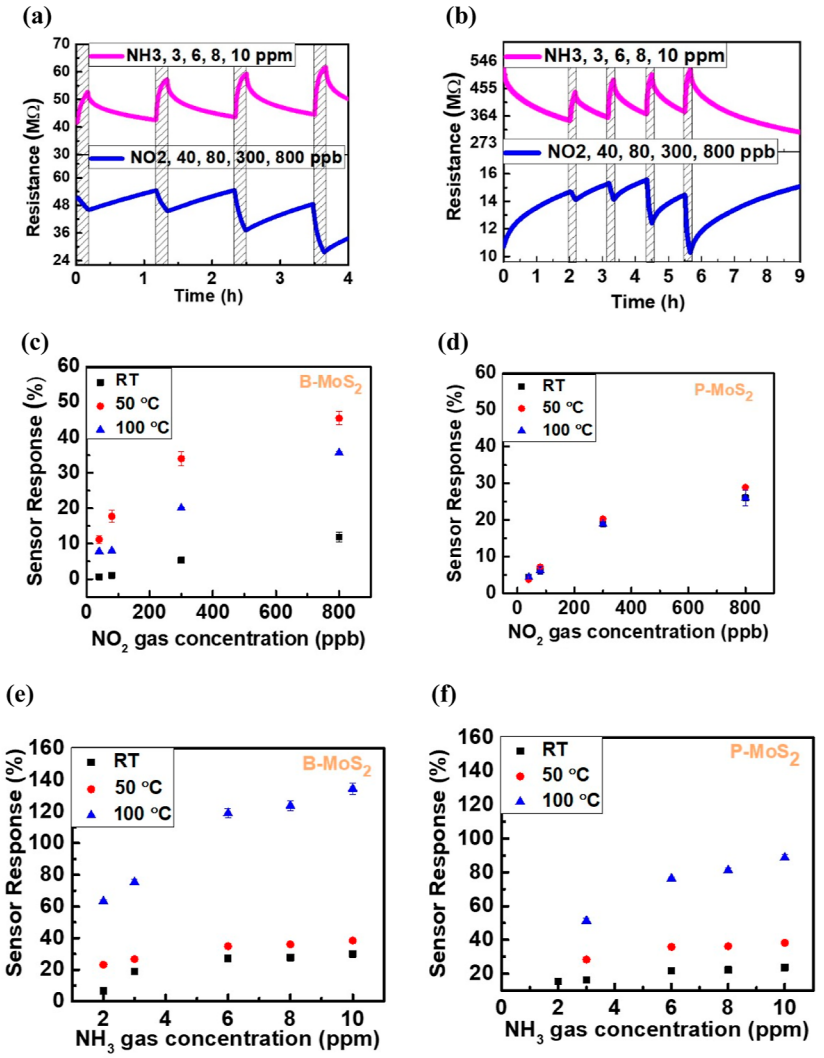

Figure 5. Variation of sensor resistance at different gas concentrations in (a) B-MoS_2 and (b) P-MoS_2 at 50 °C. The dashed bar represents the exposure time. The sensor response as a function of different values of concentration of NO_2 gas (c,d) and NH_3 gas (e,f) at room temperature, 50, and 100 °C. The left column are the results related to bath sonication MoS_2 nanoflakes (B-MoS_2), and the right column is related to probe sonication MoS_2 (P-MoS_2). Error bars represent the standard deviation of the mean value of the gas response.

monotonically decreases when the sensor is exposed to increasing nitrogen dioxide concentrations, whereas the resistance increases when the sensor is exposed to increasing ammonia vapor concentrations. In fact, NO_2 is an oxidizing gas (i.e., an acceptor of electrons); the electron charge is transferred from the MoS_2 flakes to the adsorbed gas molecules, and the resulting decrease in resistance indicates its p-type nature. Idem, NH_3 is a reducing species (i.e., electron donor), the electron charge is transferred from the adsorbed molecule to the MoS_2 material, and the increase in resistance again confirms the p-type nature of B-MoS_2 and P-MoS_2. The p-type behavior of MoS_2 nanosheets could be attributed to several reasons: substrate-induced charge transfer, charge transfer between the metal and MoS_2, the interaction between in-plane MoS_2 and the substrate oxygen adsorbed on exfoliated MoS_2.[35] Burman et al. have attributed these increases in resistance to defects that might give rise to MoO_x or MoO_3 impurities that inject holes into the MoS_2, resulting in the p-type behavior of MoS_2 sensors.[36] Most of the work reported on MoS_2 sensors prepared by liquid exfoliation using sonication showed p-type behavior.[16,30,34,37,38] The probable reason might be due to the existence of S-vacancies resulting from exfoliation during sonication, as explained previously. It was reported that the liquid exfoliation method could be a source of defects in MoS_2 nanoflakes, and the dominant defects are S-vacancies in the absence of S atoms. A S-vacancy will behave as an acceptor in the presence of ammonia vapors. Ammonia is an electron donor and thus reduces the hole concentration in the sensing layer by donating electrons, thus increasing sensor resistance.[30] Some studies reported that heating NO_2-sensor-based exfoliated MoS_2 can inverse the electrical response from the p-type behavior to the n-type by increasing the S-vacancy concentration and the partial surface oxidation of the upper MoS_2 layers in the form of MoO_3.[37,39] This was observed in our sensors when they were exposed to NO_2 but not to NH_3 or any other reducing species.

Figure S1a,b represents the complete curve, including repeatable cycles. It can be observed that the sensor response is very stable and reproducible with respect to NO_2 and NH_3 gases in both sensors. In the case of NO_2, particularly the initial cycle, the baseline was not flat, which can be due to the thermal drift, and the sensors were not able to return to their

https://doi.org/10.1021/acsomega.4c03166
ACS Omega 2024, 9, 25297−25308

Table 1. Comparison with Literature of NO_2 Gas Sensor Performance of Exfoliated MoS_2 by Bath or Probe Sonication

sonication method	solution used	substrates	type of response	temp	NO_2 response (%)	dual response	refs
probe sonication	NMP	Si_3N_4	P type	RT	0%, 1 ppm	no	37
				100 °C	21%, 1 ppm		
probe sonication	ethanol−water	SiO_2/Si	P type	RT	50%, 0.5 ppm	no	34
bath	IPA−water	Al_2O_3	P type	RT	11.87%, 0.8 ppm	yes	this work
				50 °C	45.41%, 0.8 ppm		
probe	IPA−water	Al_2O_3	P type	RT	26.02%, 0.8 ppm	yes	this work
				50 °C	28.86%, 0.8 ppm		

Table 2. Comparison with Literature of NH_3 Gas Sensor Performance of Exfoliated MoS_2 by Bath or Probe Sonication

sonication method	solution	substrates	type of response	temp	NH_3 response (%)	dual response	ref
probe	ethanol−water	SiO2/Si	P-type	RT	6%, 7 ppm	no	16,42
bath	ethanol−water	Ceramic	P-type	RT	8.525%, 50 ppm	yes	30
				150 °C	79%, 400 ppm		
bath	ethanol−water	Flexible	P-type	80 °C	15%, 50 ppm	no	36
					32%, 400 ppm		
bath	IPA−water	Al_2O_3	P type	RT	30%, 10 ppm	yes	this work
				100 °C	134%, 10 ppm		
probe	IPA−water	Al_2O_3	P type	RT	23%, 10 ppm	yes	this work
				100 °C	88%, 10 ppm		

baseline resistance with poor recovery during the cleaning phases due to the strong adsorption energy of NO_2 onto the MoS_2 material.[30,40] Nevertheless, acknowledging the critical significance of minimizing baseline drift for application, we can implement additional strategies. For instance, enhancing gas desorption by increasing flow rates, applying a moderate temperature briefly, or subjecting the sensor surface to UV light can aid in cleaning the surface.[41]

The gas sensor responses of MoS_2 bath sonication (B-MoS_2) and probe sonication (*p*-MoS_2) are presented in Figure 5c,d and e,f upon exposure to NO_2 gas in small concentrations ranging from 40 to 800 ppb and exposed to NH_3 gas from 2 to 10 ppm, respectively. Sensor response was studied for 3 different operating temperatures, i.e., RT, 50, and 100 °C. Considering the exposure to nitrogen dioxide, the highest response of the sensors was 45% (B-MoS_2) and 29% (P-MoS_2), obtained when exposed to 800 ppb (=0.8 ppm) at an operating temperature of 50 °C. For ammonia, the highest response was 134% (B-MoS_2) and 89% (P-MoS_2) at 10 ppm and an operating temperature of 100 °C. This indicates that 50 and 100 °C are the preferred operating temperatures for detecting NO_2 and NH_3, respectively, and this is regardless of the sonication method employed. The response increased from 11 to 45% for the B-MoS_2 sensor and from 4 to 29% in P-MoS_2 when NO_2 concentration increased from 40 to 800 ppb at 50 °C, whereas it increased from 75 to 134% for B-MoS_2 and 51 to 89% for P-MoS_2 when NH_3 concentration increased from 3 to 10 ppm. Both sensors were able to detect very low concentrations (as low as 40 ppb) of the NO_2 gas. Additionally, it is clearly observed in Figure 5c,d that the slope of the response at 100 °C is superior to the response at room temperature for both sensors when exposed to NH_3 gas. However, this increase in sensitivity is hardly observed between RT and 50 °C for B-MoS_2 and P-MoS_2 sensors.

Only a few results are available in the literature about dual NO_2 and NH_3 sensors using exfoliated MoS_2 obtained by the sonication method. Some examples of the performance of the NO_2 and NH_3 sensors are provided in Tables 1 and 2. These results indicate that our sensors show a reasonable response to NO_2 gas, slightly lower than the one reported for a sensor obtained by probe sonication on a silicon substrate ref 34. However, our sensors present a clearly better NH_3 response, even at RT and 100 °C, than other reported MoS_2 sensors exfoliated by bath and probe sonication. Interestingly, p type response is generally observed in exfoliated MoS_2 by probe or bath sonication, which is likely to have to do with defects in MoS_2 flakes, increasing the likelihood of the S-vacancy sites due to the exfoliation by sonication methods.[30]

The response time τ_{res} and recovery time τ_{rec} of the sensor was determined as the time required for the sensor to achieve 90% of its maximum response during exposure and 10% during recovery, respectively, as illustrated by dashed lines in Figure S2a−d. At 50 °C, the response/recovery times were approximately 461 s/6212 s (to 800 ppb of NO2) and 374 s/3248 s (to 10 ppm of NH3) for B-MoS_2, compared to 486 s/7272 and 422 s/3381 s for P-MoS_2, respectively, when exposed to NO_2 and NH_3. These values exceed those obtained at room temperature and 5 ppm of NO_2 for MoS_2 exfoliation using probe sonication.[34] Additionally, the response time increases with increasing gas concentration, while the recovery time increases with rising temperature. Burman et al.[30] reported 600 s/750 s at 70 °C, 100 ppm of NH_3 for exfoliated MoS_2 using bath sonication. In the flexible substrate, they found 158 s/385 s at 80 °C and 400 ppm of NH_3. Yao et al.[16,42] obtained a good response with no recovery. Donarelli et al.[37] reported 2220 s/1860 s at 150 °C, 1 ppm of NO_2. To optimize the gas sensor performance by reducing exposure and recovery time, heterostructures, hybridization, and functionalization can be explored.[43] Liu et al.[44] reported a 276 s recovery time in MoS_2/ZnS heterostructure compared to over 4800 s in pure MoS_2 at 25 °C, 5 ppm of NO_2. Han et al.[45] reported a 74 s response time in MoS_2/SnO_2 heterostructures instead of 165 s in pure MoS_2 at room temperature, 5 ppm of NO2. Furthermore, it was demonstrated that the incorporation of carbon dots improved the MoS_2 response time of the humidity sensor.[46]

Figure S2e,f represents the response and recovery times of MoS_2 bath sonication (B-MoS_2) and probe sonication (P-

https://doi.org/10.1021/acsomega.4c03166
ACS Omega 2024, 9, 25297−25308

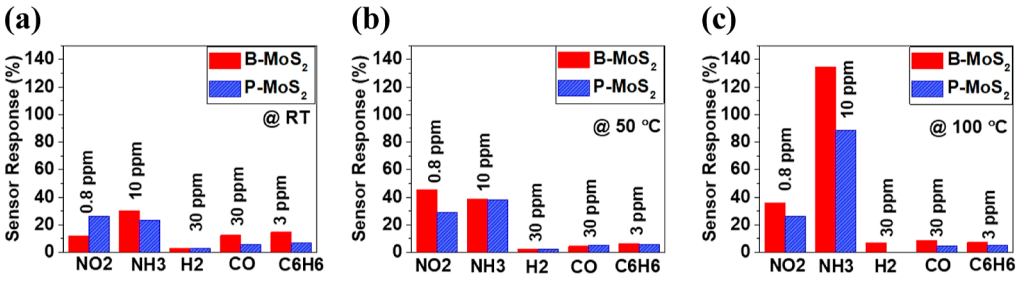

Figure 6. Selectivity analysis of exfoliated MoS_2 (a) at room temperature, (b) 50, and (c) 100 °C.

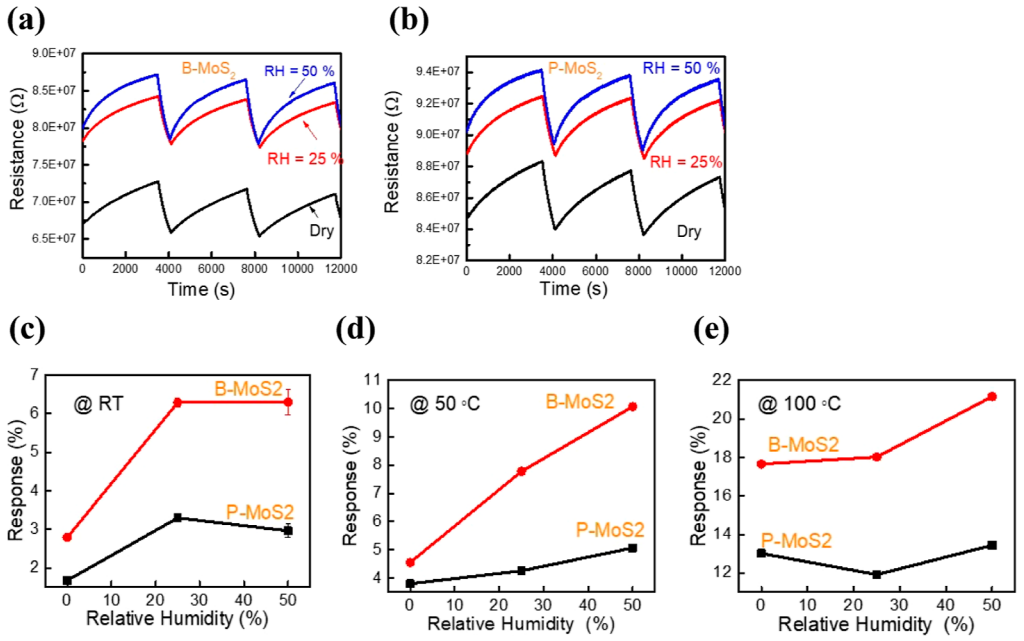

Figure 7. Transient response and recovery of (a) B-MoS_2 and (b) P-MoS_2 sensor for the low humidity level (RH = 25%) and the high humidity level (RH = 50%) at 50 °C. The gas sensor response to 0.8 ppm of NO_2 from dry to humid conditions in three temperature values (c) room temperature, (d) 50, and (e) 100 °C.

MoS_2) when exposed to 800 ppb of NO_2 gas and 10 ppm of NH_3 gas at three different temperatures. It is evident that temperature affects the response and recovery time, as shown in Figure S2e,f. In the case of the B-MoS_2 sensor (Figure S2e), as the temperature increases from 50 to 100 °C, the response time increases by 38 and 70 s when exposed to NO_2 and NH_3, respectively, while the recovery time decreases by 3492 and 914 s when exposed to NO_2 and NH_3, respectively. However, for the P-MoS_2 sensor (Figure S2f), as the temperature rises from 50 to 100 °C, both the response and recovery times decrease by 214 s/6643 and 113 s/1851 s when exposed to NO_2 and NH_3, respectively. This is attributed to the thermal energy generated at high temperatures, inducing reduction of defects on the surface and accelerating the desorption of absorbed gas.[34,47]

The long-term stability of sensors was investigated, as illustrated in Figure S3a,b, where different concentrations of NO_2 gas were monitored over a 43-day period. Notably, the P-MoS_2 sensors exhibited a consistent and stable response throughout the duration of the experiment. In contrast, the B-MoS_2 sensor displayed a degradation ranging from 22 to 32% over the same period, indicating a decline in its stability. This discrepancy in stability can be attributed to the structural disparities between the two sensors. The P-MoS_2 sensors, characterized by thicker and smaller flakes, demonstrated resilience and durability over prolonged exposure. Conversely, the thinner and larger flakes of B-MoS_2 sensors contributed to their diminished stability over time.

2.6. Selectivity. Selectivity is another important parameter in gas sensing. Figure 6 presents the selectivity of the B-MoS_2 and P-MoS_2 to nitrogen dioxide, NO_2, ammonia, NH_3, hydrogen, H_2, carbon monoxide, CO, and benzene, C_6H_6, target gases. It shows that the selectivity of both sensors depends on the temperature. At 50 °C (Figure 6b), B-MoS_2 and P-MoS_2 are selective for NO_2 and NH_3. At 100 °C (Figure 6c), both sensors, and especially B-MoS_2, are selective for NH_3 gas. Surprisingly, the B-MoS_2 sensor, which has bigger flakes, exhibits better response and selectivity compared to P-MoS_2. Hau et al.[34] have reported that MoS_2 nanosheets formed by probe sonication are selective for only NO_2 at room temperature. Our samples showed dual selectivity at RT and 50 °C with better selectivity to NH_3 at 100 °C in both sensors, considering that the NO_2 response is decreasing at 100 °C in comparison to the response at 50 °C.

2.7. Humidity. In general, humidity is one of the enemies of gas sensors. In order to study the effect of humidity on our sensing response, humidity sensing was evaluated with two relative humidity (RH) values equal to 25 and 50% for both sensors while applying 0.8 ppm of NO_2 gas. Figure 7a,b shows the resistance variation of the sensor in dry and humid

https://doi.org/10.1021/acsomega.4c03166
ACS Omega 2024, 9, 25297−25308

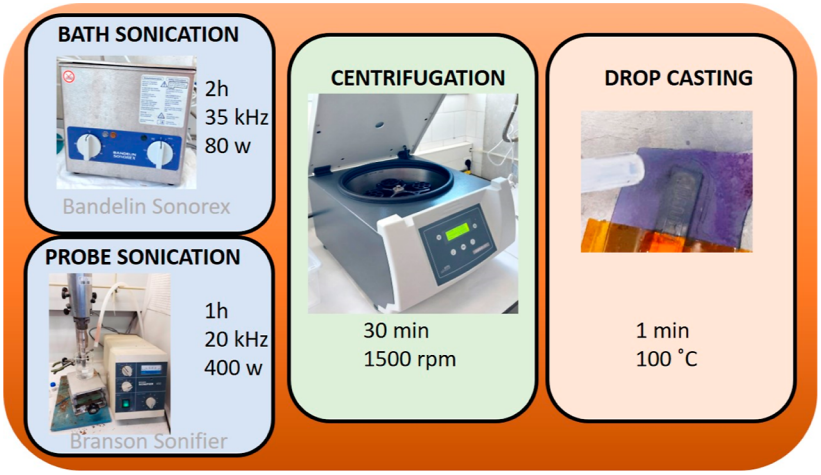

Figure 8. Overview of MoS_2 synthesis steps and conditions for preparing chemo resistive gas sensors.

conditions. We observe an increase of the baseline resistance of the sensor in contact with humidity from 6.7 to 8 MΩ for B-MoS_2 and 8.5 to 9 MΩ for P-MoS_2, and the resistance retains its p-type semiconducting behavior. Therefore, the holes are the majority of charge carriers for both devices, and since the adsorbed water molecules react as electron donors, the conductivity decreases and the baseline resistance increases in both sensors.[48,49] Figure 7c–e represents the response toward NO_2 gas from a dry to a humid condition at room temperature, 50, and 100 °C. We observe that the response toward NO_2 at RT is quite remarkable, NO_2 response at RT does not change when humidity varies between 25 and 50% in both sensors. This means that the sensors operated at RT show a NO_2 response quite independent of changes in moisture levels. However, an increase of response in the presence of humidity in both sensors is observed, and this enhancement in response is more present at the operating temperature of 50 °C and reaches 5.5% in B-MoS_2 and 3% in P-MOS_2 compared to room temperature and 100 °C. This enhancement could be explained by considering the interactions between the MoS_2 surface, NO_2, and water molecules as follows: (1) competitive adsorption of the water molecules with NO_2 molecules for adsorption sites on the MoS_2 surface. In humid conditions, some of the active sites on the MoS_2 surface might be occupied by water molecules, limiting the available sites for NO_2 adsorption. However, if the MoS_2 surface has as higher affinity for NO_2 than for water, water might be displaced by NO_2 at these active sites, leading to an increased response.[50] (2) Surface chemistry, while the presence of water vapor can lead to the formation of hydroxyl groups (OH^-) on the MoS_2 surface and create additional adsorption sites for NO_2 molecules interacting with the MoS_2 surface, leading to a higher sensor response.[51]

2.8. Sensing Mechanism. While MoS_2 nanoflakes produced from probe sonication exhibit smaller size, greater rugosities, and structural damage compared to those from bath sonication, their sensing mechanism remains consistent. However, probe sonication may introduce more defects, including S-vacancies, onto the MoS_2 surface. These vacancies act as acceptors in the presence of gas, trapping analyte molecules at these sites. Both bath and probe sonication demonstrate a p-type response in sensing. The gas sensing mechanism of exfoliated MoS_2 involves surface oxygen adsorption and charge transfer. Previous studies have identified O_2^- as the predominant type of oxygen ion in temperature ranging from RT to 150 °C. Upon exposure to NO_2 gas, the p-type MoS_2 semiconductor absorbs NO_2 molecules onto its surface, extracting electrons from the valence band and interacting with oxygen ion O_2^- ($O_2 + e^- \rightarrow O_2^-$) and S vacancies. This process increases hole concentration and reduces sensor resistance (eqs 1–3). Furthermore, B-MoS_2 exhibits a larger specific surface area compared to P-MoS_2 when interacting with the NO_2 gas. This increase in active adsorption sites enhances the NO_2 sensing response, providing an improved capability for detecting NO_2 gas.[8,34,37,52]

$$NO_2 + e^- \rightarrow NO_2^- \quad (1)$$

$$NO_2 + O_2^- + 2e^- \rightarrow NO_2^- + 2O^- \quad (2)$$

$$NO_2 + VS^{++} \rightarrow NO_2 + h^+ \quad (3)$$

When a p-type MoS_2 semiconductor is exposed to NH_3 gas, the NH_3 molecule acts as an electron donor, decreasing the hole concentration on the MoS_2 surface by donating electrons. Consequently, this process increases the sensor resistance. Previous works have described the potential reactions that might occur, as depicted in eqs 4 and 5[30]

$$4NH_3 + 5O_2^- \rightarrow 4NO + 6H_2O + 5e^- \quad (4)$$

$$4NH_3 + 3O_2^- \rightarrow 2N_2 + 6H_2O + 3e^- \quad (5)$$

3. CONCLUSIONS

MoS_2 gas sensors were prepared by sonication-assisted liquid exfoliation using either the bath or probe sonication method. The structural characterizations, FSEM, HRTEM, and DSL, of the exfoliated material showed a clearly large lateral size of the nanoflakes up to 2 μm by bath sonication compared to the probe sonication method. Raman and AFM confirmed their exfoliation into multilayer nanoflakes. The gas sensor measurements showed competitive results between B-MoS_2 and P-MoS_2 using environmentally friendly solutions within a reasonable time of preparation for detecting NO_2 and NH_3 toxic gases at room temperature, 50, and 100 °C. Gas sensing experiments reveal that the MoS_2 nanoflakes prepared via indirect sonication enhanced responsivity by 17 and 46% toward NO_2 and NH_3 gases, respectively, compared to the direct sonication method. We demonstrated that both sensors are highly selective toward NO_2 and NH_3 gas with respect to

https://doi.org/10.1021/acsomega.4c03166
ACS Omega 2024, 9, 25297−25308

H_2, CO, and benzene. Room temperature enables the detection of NO_2 with very good resilience to changes in humidity levels. Moreover, at higher operating temperatures (yet moderate), NH_3 detection is enhanced. Overall, this study reveals that the method of sonication influences gas sensor performance, and the bath sonication method is recommended for achieving better gas sensor response.

4. EXPERIMENTAL SECTION

4.1. Preparation of MoS_2 Solution. MoS_2 dispersion was prepared using 10 mg of bulk powder obtained from SIGMA Aldrich reference n 234842-100G. To formulate the dispersions at specific concentrations, MoS_2 powders were weighted using a KERN ADJ balance, which were then mixed in 3 mL of isopropanol solvent and 7 mL of DI water obtained from Sigma-Aldrich. Bath sonication was conducted in glass vials using a Bandelin Sonorex ultrasonic bath (frequency: 35 kHz, power: 80 W) and then placed on plastic vials for centrifuging. Probe sonication was handled by a Branson Sonifier model 450 (frequency: 20 kHz, power 400 W) equipped with a Ti alloy tapped horn tip (diameter: 13 mm) and was dipped in a plastic tube (diameter: 15 mm). The pulsed mode was used to minimize heat generation with 40% duty cycle (30% on, 70% off) output control in position 7. To avoid heating the solution and evaporation of the solvent, a vial tube was placed inside a beaker with ice−water.

Centrifugation was performed in the same vials using a Digicen 21 (model RT267) centrifuge at 1500 rpm (377 rcf) during 30 min (Figure 8).

4.2. MoS_2 Sensor Preparation. To obtain sensing devices, the suspensions in solvents were drop-cast onto the 8 × 4 mm interdigitated electrode area of alumina transducing substrates (Ceramtech). At first, the transducing substrates were cleaned sequentially for 15 min in acetone, IPA, and DI water in the sonication bath. Then, a pipet was used to collect and separate the suspension (taken from the MoS_2 sediment). Pipette-captured 0.25 mL drops were cast onto the electrodes of the alumina substrates and dried for 1 min on a hot plate at 100 °C (Figure 8).

The sensor is placed inside a homemade Teflon gas chamber. This sensing chamber is connected to a gas mixer and delivery systems that use calibrated cylinders and pure air as a balance and carrier gas. The total concentrations of nitrogen dioxide, NO_2, ammonia, NH_3, hydrogen, H_2, carbon monoxide, CO, and benzene, C_6H_6, are respectively 1 ppm, 100 ppm, 1000, 100, and 100 ppm. To set different gas concentrations, the gas cylinder is diluted in synthetic dry air (purity 99.995%) by multigas mass flow controllers (Bronkhorst) and connected to a computer equipped with a software tool for monitoring flow-bus parameter values. The total flow into the chamber is kept constant at 100 mL/min. The sensor is connected to a Keysight DAQ970A data acquisition system to record the changes in sensor resistance upon exposure to the gas flow. The Keysight BenchVue Data Acquisition software allows acquiring and recording measurement data and performing real-time display and analysis of the measurement results. The backside heater printed on the alumina transducers is used to set different operation temperatures up to 200 °C. The temperature is controlled manually by the power supply. When the temperature is stable, the measurement is acquired, and the sample is exposed for 1 h to synthetic air (recovery or desorption time) to purge the chamber before applying gas for 10 min (exposure or adsorption time). To verify the short-term stability of the sensor response, seven repetitions are recorded. Error bars represent the standard deviation of the mean value of the gas response calculated from the last three cycles obtained. Initially, after the modification of the gas, we expose the sensors to dry air overnight before starting the measurement to clean the sensor surface. When we increase the temperature from RT to 50 °C and then to 100 °C, the baseline resistance of the sensors decreases due to the semiconducting nature of MoS_2 nanoflakes.[34] The measurement is recorded when the baseline resistance reaches its final value, mostly after 1 h.

The sensor response of the gas sensor is expressed in percent and was calculated from the following definition: $\left|\frac{R_{air}-R_{gas}}{R_{air}}\right| \times 100$, where R_{gas} and R_{air} are the resistance of the sensor exposed to gas and synthetic air, respectively. Its sign is related to the direction of resistance change upon exposure to oxidizing or reducing gaseous species.

■ ASSOCIATED CONTENT

Supporting Information

The Supporting Information is available free of charge at https://pubs.acs.org/doi/10.1021/acsomega.4c03166.

Short-term stability and repeatability of sensor resistance at different gas concentrations in B-MoS_2 and P-MoS_2 sensors at 50 °C, response time τ_{res} and recovery time τ_{rec} of B-MoS_2 and P-MoS_2 at 50 °C toward 800 ppb NO_2 and 10 ppm of NH_3 gas, response time and recovery time versus temperature of B-MoS_2 and P-MoS_2 sensors, respectively, and long-term stability of the B-MoS_2 and P-MoS_2 sensors for different concentrations of NO_2 gas at 100 °C (PDF)

■ AUTHOR INFORMATION

Corresponding Author

Dalal Fadil − *Departament d'Enginyeria Electrònica, Universitat Rovira i Virgili, Tarragona 43007, Spain;* orcid.org/0000-0002-2369-5074; Email: dalal.fadil@urv.cat

Authors

Jyayasi Sharma − *Departament d'Enginyeria Electrònica, Universitat Rovira i Virgili, Tarragona 43007, Spain*

Mubdiul Islam Rizu − *Departament d'Enginyeria Electrònica, Universitat Rovira i Virgili, Tarragona 43007, Spain;* orcid.org/0000-0002-4728-3672

Eduard Llobet − *Departament d'Enginyeria Electrònica, Universitat Rovira i Virgili, Tarragona 43007, Spain;* orcid.org/0000-0001-6164-4342

Complete contact information is available at: https://pubs.acs.org/10.1021/acsomega.4c03166

Notes

The authors declare no competing financial interest.

■ ACKNOWLEDGMENTS

This project has received funding from the European Union's Horizon 2020 research and innovation programme under the Marie Sokolowski-Curie grant agreements nos. 101025770 and 945413. We thank AGAUR-FI SDUR (2022 FI SDUR 00307) and the department of Research and Universities of the Generalitat of Catalonia and the European Social Fund Plus.

We would like to thank URV's technician staff for their help in FESEM, TEM, AFM, and XRD as well as URV's chemical department (Dr. Yolanda Cesteros) for sharing the probe sonication. E.L. is supported by the Catalan Institution for Research and Advanced Studies via the 2023 edition of the ICREA Academia Award.

REFERENCES

(1) Park, S. Y.; Kim, Y.; Kim, T.; Eom, T. H.; Kim, S. Y.; Jang, H. W. Chemoresistive Materials for Electronic Nose: Progress, Perspectives, and Challenges. *InfoMat* **2019**, *1* (3), 289−316.
(2) Khatib, M.; Haick, H. Sensors for Volatile Organic Compounds. *ACS Nano* **2022**, *16*, 7080−7115.
(3) Zhou, X.; Xue, Z.; Chen, X.; Huang, C.; Bai, W.; Lu, Z.; Wang, T. Nanomaterial-Based Gas Sensors Used for Breath Diagnosis. *J. Mater. Chem. B* **2020**, *8* (16), 3231−3248.
(4) Muthumalai, K.; Gokila, N.; Haldorai, Y.; Rajendra Kumar, R. T. Nanosensors for Crop Protection: Design and Fabrication. *Nanosensors for Smart Agriculture*; Elsevier, 2021.
(5) Halfaya, Y.; Bishop, C.; Soltani, A.; Sundaram, S.; Aubry, V.; Voss, P.; Salvestrini, J.-P.; Ougazzaden, A. Investigation of the Performance of HEMT-Based NO, NO2 and NH3 Exhaust Gas Sensors for Automotive Antipollution Systems. *Sensors* **2016**, *16* (3), 273.
(6) Tang, H.; Sacco, L. N.; Vollebregt, S.; Ye, H.; Fan, X.; Zhang, G. Recent Advances in 2D/Nanostructured Metal Sulfide-Based Gas Sensors: Mechanisms, Applications, and Perspectives. *J. Mater. Chem. A* **2020**, *8* (47), 24943−24976.
(7) Buckley, D. J.; Black, N. C. G.; Castanon, E. G.; Melios, C.; Hardman, M.; Kazakova, O. Frontiers of Graphene and 2D Material-Based Gas Sensors for Environmental Monitoring. *2D Mater.* **2020**, *7* (3), 032002.
(8) Yang, S.; Jiang, C.; Wei, S. Gas Sensing in 2D Materials. *Appl. Phys. Rev.* **2017**, *4* (2), 021304.
(9) Dai, J.; Ogbeide, O.; Macadam, N.; Sun, Q.; Yu, W.; Li, Y.; Su, B. L.; Hasan, T.; Huang, X.; Huang, W. Printed Gas Sensors. *Chem. Soc. Rev.* **2020**, *49* (6), 1756−1789.
(10) Wang, Z.; Bu, M.; Hu, N.; Zhao, L. An Overview on Room-Temperature Chemiresistor Gas Sensors Based on 2D Materials: Research Status and Challenge. *Composites, Part B* **2023**, *248* (September 2022), 110378.
(11) Chhowalla, M.; Shin, H. S.; Eda, G.; Li, L. J.; Loh, K. P.; Zhang, H. The Chemistry of Two-Dimensional Layered Transition Metal Dichalcogenide Nanosheets. *Nat. Chem.* **2013**, *5* (4), 263−275.
(12) Coleman, J. N.; Lotya, M.; O'Neill, A.; Bergin, S. D.; King, P. J.; Khan, U.; Young, K.; Gaucher, A.; De, S.; Smith, R. J.; Shvets, I. V.; Arora, S. K.; Stanton, G.; Kim, H. Y.; Lee, K.; Kim, G. T.; Duesberg, G. S.; Hallam, T.; Boland, J. J.; Wang, J. J.; Donegan, J. F.; Grunlan, J. C.; Moriarty, G.; Shmeliov, A.; Nicholls, R. J.; Perkins, J. M.; Grieveson, E. M.; Theuwissen, K.; McComb, D. W.; Nellist, P. D.; Nicolosi, V. Two-Dimensional Nanosheets Produced by Liquid Exfoliation of Layered Materials. *Science* **2011**, *331* (6017), 568−571.
(13) Smith, R. J.; King, P. J.; Lotya, M.; Wirtz, C.; Khan, U.; De, S.; O'Neill, A.; Duesberg, G. S.; Grunlan, J. C.; Moriarty, G.; Chen, J.; Wang, J.; Minett, A. I.; Nicolosi, V.; Coleman, J. N. Large-Scale Exfoliation of Inorganic Layered Compounds in Aqueous Surfactant Solutions. *Adv. Mater.* **2011**, *23* (34), 3944−3948.
(14) O'Neill, A.; Khan, U.; Coleman, J. N. Preparation of High Concentration Dispersions of Exfoliated MoS 2 with Increased Flake Size. *Chem. Mater.* **2012**, *24* (12), 2414−2421.
(15) Mellado, C.; Figueroa, T.; Baez, R.; Meléndrez, M.; Fernández, K. Effects of Probe and Bath Ultrasonic Treatments on Graphene Oxide Structure. *Mater. Today Chem.* **2019**, *13*, 1−7.
(16) Yao, Y.; Tolentino, L.; Yang, Z.; Song, X.; Zhang, W.; Chen, Y.; Wong, C. P. High-Concentration Aqueous Dispersions of MoS2. *Adv. Funct. Mater.* **2013**, *23* (28), 3577−3583.
(17) Alzakia, F. I.; Jonhson, W.; Ding, J.; Tan, S. C. Ultrafast Exfoliation of 2D Materials by Solvent Activation and One-Step Fabrication of All-2D-Material Photodetectors by Electrohydrodynamic Printing. *ACS Appl. Mater. Interfaces* **2020**, *12* (25), 28840−28851.
(18) Taghavi, N. S.; Afzalzadeh, R. The Effect of Sonication Parameters on the Thickness of the Produced MoS2 Nano-Flakes. *Arch. Acoust.* **2021**, *46* (1), 31−40.
(19) Fadil, D.; Hossain, R. F.; Saenz, G. A.; Kaul, A. B. On the Chemically-Assisted Excitonic Enhancement in Environmentally-Friendly Solution Dispersions of Two-Dimensional MoS2 and WS2. *J. Mater. Chem. C* **2017**, *5* (22), 5323−5333.
(20) Yang, L.; Cui, X.; Zhang, J.; Wang, K.; Shen, M.; Zeng, S.; Dayeh, S. A.; Feng, L.; Xiang, B. Lattice Strain Effects on the Optical Properties of MoS2 Nanosheets. *Sci. Rep.* **2014**, *4* (1), 5649.
(21) Khan, M.; Kumar, S.; Mishra, A.; Sulania, I.; Nath Tripathi, M.; Tripathi, A. Materials Today: Proceedings Study of Structural and Electronic Properties of Few-Layer MoS 2 Film. *Mater. Today: Proc.* **2022**, *57*, 100−105.
(22) Pandey, A.; Dutta, S.; Kumar, A.; Raman, R.; K Kapoor, A.; Muralidhran, R. Structural and Optical Properties of Bulk MoS2 for 2D Layer Growth. *Adv. Mater. Lett.* **2016**, *7* (10), 777−782.
(23) Jadkar, V.; Pawbake, A.; Waykar, R.; Jadhavar, A.; Mayabadi, A.; Date, A.; Late, D.; Pathan, H.; Gosavi, S.; Jadkar, S. Synthesis of Orthorhombic-Molybdenum Trioxide (α-MoO3) Thin Films by Hot Wire-CVD and Investigations of Its Humidity Sensing Properties. *J. Mater. Sci.: Mater. Electron.* **2017**, *28* (21), 15790−15796.
(24) Lamouchi, A.; Assaker, I. B.; Chtourou, R. Effect of Annealing Temperature on the Structural, Optical, and Electrical Properties of MoS2 Electrodeposited onto Stainless Steel Mesh. *J. Mater. Sci.* **2017**, *52* (8), 4635−4646.
(25) Baby, M.; Rajeev Kumar, K. Structural and Optical Characterization of Stacked MoS2 Nanosheets by Hydrothermal Method. *J. Mater. Sci.: Mater. Electron.* **2018**, *29* (6), 4658−4667.
(26) Tye, C. T.; Smith, K. J. Cold Lake Bitumen Upgrading Using Exfoliated MoS 2. *Catal. Lett.* **2004**, *95* (3/4), 203−209.
(27) Li, H.; Zhang, Q.; Yap, C. C. R.; Tay, B. K.; Edwin, T. H. T.; Olivier, A.; Baillargeat, D. From Bulk to Monolayer MoS 2: Evolution of Raman Scattering. *Adv. Funct. Mater.* **2012**, *22* (7), 1385−1390.
(28) Lee, C.; Yan, H.; Brus, L. E.; Heinz, T. F.; Hone, J.; Ryu, S. Anomalous Lattice Vibrations of Single- and Few-Layer MoS2. *ACS Nano* **2010**, *4* (5), 2695−2700.
(29) Chakraborty, B.; Matte, H. S. S. R.; Sood, A. K.; Rao, C. N. R. Layer-Dependent Resonant Raman Scattering of a Few Layer MoS2. *J. Raman Spectrosc.* **2013**, *44* (1), 92−96.
(30) Burman, D.; Ghosh, R.; Santra, S.; Kumar Ray, S.; Kumar Guha, P. Role of Vacancy Sites and UV-Ozone Treatment on Few Layered MoS2 Nanoflakes for Toxic Gas Detection. *Nanotechnology* **2017**, *28* (43), 435502.
(31) Mak, K. F.; Lee, C.; Hone, J.; Shan, J.; Heinz, T. F. Atomically Thin MoS_2: A New Direct-Gap Semiconductor. *Phys. Rev. Lett.* **2010**, *105* (13), 136805.
(32) Ramasubramaniam, A. Large Excitonic Effects in Monolayers of Molybdenum and Tungsten Dichalcogenides. *Phys. Rev. B: Condens. Matter Mater. Phys.* **2012**, *86* (11), 115409−115416.
(33) Rodriguez, C. L. C.; Muñoz, P. A. R.; Donato, K. Z.; Seixas, L.; Donato, R. K.; Fechine, G. J. M. Understanding the Unorthodox Stabilization of Liquid Phase Exfoliated Molybdenum Disulfide (MoS 2) in Water Medium. *Phys. Chem. Chem. Phys.* **2020**, *22* (3), 1457−1465.
(34) Hau, H. H.; Duong, T. T. H.; Man, N. K.; Thi Viet Nga, T.; Thi Xuan, C.; Thi Thanh Le, D.; Van Toan, N.; Hung, C. M.; Van Duy, N.; Van Hieu, N.; Hoa, N. D. Enhanced NO2 Gas-Sensing Performance at Room Temperature Using Exfoliated MoS2 Nanosheets. *Sens. Actuators, A* **2021**, *332*, 113137.
(35) Han, Y.; Huang, D.; Ma, Y.; He, G.; Hu, J.; Zhang, J.; Hu, N.; Su, Y.; Zhou, Z.; Zhang, Y.; Yang, Z. Design of Hetero-Nanostructures on MoS_2 Nanosheets To Boost NO_2 Room-Temperature Sensing. *ACS Appl. Mater. Interfaces* **2018**, *10* (26), 22640−22649.

https://doi.org/10.1021/acsomega.4c03166
ACS Omega 2024, 9, 25297−25308

(36) Burman, D.; Sharma, A.; Guha, P. K. Flexible Large MoS 2 Film Based Ammonia Sensor. *IEEE Sens. Lett.* **2018**, *2* (2), 1−4.
(37) Donarelli, M.; Prezioso, S.; Perrozzi, F.; Bisti, F.; Nardone, M.; Giancaterini, L.; Cantalini, C.; Ottaviano, L. Response to NO2 and Other Gases of Resistive Chemically Exfoliated MoS2-Based Gas Sensors. *Sens. Actuators, B* **2015**, *207*, 602−613.
(38) Ren, Z.; Shi, Y.; Song, T.; Wang, T.; Tang, B.; Niu, H.; Yu, X. Flexible Low-Temperature Ammonia Gas Sensor Based on Reduced Graphene Oxide and Molybdenum Disulfide. *Chemosensors* **2021**, *9* (12), 345.
(39) Cantalini, C.; Giancaterini, L.; Donarelli, M.; Santucci, S.; Ottaviano, L. P2.8.4 NO2 Response to Few-Layers MoS2. In *Proceedings IMCS 2012*; AMA Service GmbH: Von-Münchhausen-Str. 49, 31515: Wunstorf, Germany, 2012; pp 1656−1659.
(40) Annanouch, F. E.; Alagh, A.; Umek, P.; Casanova-Chafer, J.; Bittencourt, C.; Llobet, E. Controlled Growth of 3D Assemblies of Edge Enriched Multilayer MoS2 Nanosheets for Dually Selective NH3 and NO2 Gas Sensors. *J. Mater. Chem. C* **2022**, *10* (30), 11027−11039.
(41) Casanova-Chafer, J.; Garcia-Aboal, R.; Llobet, E.; Atienzar, P. Enhanced CO 2 Sensing by Oxygen Plasma-Treated Perovskite−Graphene Nanocomposites. *ACS Sens.* **2024**, *9*, 830−839.
(42) Yao, Y.; Lin, Z.; Li, Z.; Song, X.; Moon, K. S.; Wong, C. P. Large-Scale Production of Two-Dimensional Nanosheets. *J. Mater. Chem.* **2012**, *22* (27), 13494−13499.
(43) Kim, Y.; Sohn, I.; Shin, D.; Yoo, J.; Lee, S.; Yoon, H.; Park, J.; Chung, S.; Kim, H. Recent Advances in Functionalization and Hybridization of Two-Dimensional Transition Metal Dichalcogenide for Gas Sensor. *Adv. Eng. Mater.* **2024**, *26* (1), 2301063.
(44) Liu, C.; Chen, X.; Luo, H.; Li, B.; Shi, J.; Fan, C.; Yang, J.; Zeng, M.; Zhou, Z.; Hu, N.; Su, Y.; Yang, Z. Highly Sensitive and Recoverable Room-Temperature NO2 Gas Detection Realized by 2D/0D MoS2/ZnS Heterostructures with Synergistic Effects. *Sens. Actuators, B* **2021**, *347* (2), 130608.
(45) Han, Y.; Ma, Y.; Liu, Y.; Xu, S.; Chen, X.; Zeng, M.; Hu, N.; Su, Y.; Zhou, Z.; Yang, Z. Construction of MoS2/SnO2 Heterostructures for Sensitive NO2 Detection at Room Temperature. *Appl. Surf. Sci.* **2019**, *493* (June), 613−619.
(46) He, G.; Huang, D.; Yang, Z.; Han, Y.; Hu, J.; Hu, N.; Su, Y.; Zhou, Z.; Zhang, Y.; Zhang, Y. Linear Humidity Response of Carbon Dot-Modified Molybdenum Disulfide. *Phys. Chem. Chem. Phys.* **2018**, *20* (6), 4083−4091.
(47) Thang, N. T.; Hong, L. T.; Thoan, N. H.; Hung, C. M.; Van Duy, N.; Van Hieu, N.; Hoa, N. D. Controlled Synthesis of Ultrathin MoS2 Nanoflowers for Highly Enhanced NO2 Sensing at Room Temperature. *RSC Adv.* **2020**, *10* (22), 12759−12771.
(48) Burman, D.; Kumar Jha, R.; Santra, S.; Kumar Guha, P. Exfoliated MoS2 Based Humidity Sensing. *Adv. Mater. Proc.* **2021**, *1* (2), 176−179.
(49) Zhang, S. L.; Jung, H.; Huh, J. S.; Yu, J. B.; Yang, W. C. Efficient Exfoliation of MoS2with Volatile Solvents and Their Application for Humidity Sensor. *J. Nanosci. Nanotechnol.* **2014**, *14* (11), 8518−8522.
(50) Cao, J.; Chen, Q.; Wang, X.; Zhang, Q.; Yu, H.-D.; Huang, X.; Huang, W. Recent Development of Gas Sensing Platforms Based on 2D Atomic Crystals. *Research* **2021**, *2021*, 9863038.
(51) Burman, D.; Ghosh, R.; Santra, S.; Guha, P. K. Highly Proton Conducting MoS 2/Graphene Oxide Nanocomposite Based Chemo-resistive Humidity Sensor. *RSC Adv.* **2016**, *6* (62), 57424−57433.
(52) Cho, B.; Hahm, M. G.; Choi, M.; Yoon, J.; Kim, A. R.; Lee, Y. J.; Park, S. G.; Kwon, J. D.; Kim, C. S.; Song, M.; Jeong, Y.; Nam, K. S.; Lee, S.; Yoo, T. J.; Kang, C. G.; Lee, B. H.; Ko, H. C.; Ajayan, P. M.; Kim, D. H. Charge-Transfer-Based Gas Sensing Using Atomic-Layer MoS2. *Sci. Rep.* **2015**, *5* (1), 8052.

https://doi.org/10.1021/acsomega.4c03166
ACS Omega 2024, 9, 25297−25308